Exploring the Energy Spectrum of a Four-Terminal Josephson Junction: Toward Topological Andreev Band Structures

Tommaso Antonelli,[1,2,*] Marco Coraiola,[1,*] David Christian Ohnmacht,[3] Aleksandr E. Svetogorov,[3]
Deividas Sabonis,[1] Sofieke C. ten Kate,[1] Erik Cheah,[2] Filip Krizek,[2] Rüdiger Schott,[2] Juan Carlos Cuevas,[4,5]
Wolfgang Belzig,[3] Werner Wegscheider,[2] and Fabrizio Nichele[1,†]
[1]*IBM Research Europe-Zurich, 8803 Rüschlikon, Switzerland*
[2]*Laboratory for Solid State Physics, ETH Zürich, 8093 Zürich, Switzerland*
[3]*Fachbereich Physik, Universität Konstanz, D-78457 Konstanz, Germany*
[4]*Departamento de Física Teórica de la Materia Condensada, Universidad Autónoma de Madrid, 28049 Madrid, Spain*
[5]*Condensed Matter Physics Center (IFIMAC), Universidad Autónoma de Madrid, 28049 Madrid, Spain*

(Received 14 January 2025; revised 5 May 2025; accepted 7 August 2025; published 9 September 2025)

Hybrid multiterminal Josephson junctions (JJs) are expected to harbor a novel class of Andreev bound states (ABSs), including topologically nontrivial states in four-terminal devices. In these systems, topological phases emerge when ABSs depend on at least three superconducting phase differences, resulting in a three-dimensional (3D) energy spectrum characterized by Weyl nodes at zero energy. Here, we realize a four-terminal JJ in a hybrid Al/InAs heterostructure, where ABSs form a synthetic 3D band structure. We probe the energy spectrum using tunneling spectroscopy and identify spectral features associated with the formation of a tri-Andreev molecule, a bound state whose energy depends on three superconducting phases and, therefore, is able to host topological ABSs. The experimental observations are well described by a numerical model. The calculations predict the appearance of four Weyl nodes at zero energy within a gap smaller than the experimental resolution. These topological states are theoretically predicted to remain stable within an extended region of the parameter space, well accessible by our device. These findings establish an experimental foundation to study high-dimensional synthetic band structures in multiterminal JJs and to realize topological Andreev bands.

DOI: 10.1103/qd3y-f912 Subject Areas: Condensed Matter Physics

I. INTRODUCTION

Josephson junctions (JJs) are key elements of superconducting circuits, used in quantum technology applications and fundamental research. In a superconducting–normal conductor–superconducting junction, supercurrent transport is mediated by Andreev bound states (ABSs), electron-hole superposition states confined within the normal area. The ABS energy depends on the phase difference between the superconducting wave functions of the two leads [1–4]. Recently, these electronic modes have been the subject of extensive study [5–12], including the coherent manipulation of ABSs [13–16] and the exploration of topological superconductivity [17–20].

In multiterminal JJs (MTJJs), where three or more superconducting terminals are linked to a single normal scattering region, ABSs form synthetic band structures which are expected to host a wide range of properties not attainable in two-terminal devices. Among the most intriguing prospects is the potential to realize topologically nontrivial phases in the three-dimensional (3D) band structure of four-terminal JJs (4TJJs), with Weyl nodes arising in the energy spectrum [21–27]. Topological phases in these systems are inherently robust with respect to external perturbations [21], making them particularly appealing for applications in quantum information processing [28,29] and spintronics [30].

A first set of studies on MTJJs focused on their transport properties, including the signatures of Cooper pair quartets [31–35] and the flow of supercurrents across multiple superconducting leads [36–42]. Recently, MTJJs have been proposed as a platform to realize Andreev molecules—a system where ABSs hybridize due to the spatial overlap of their wave functions [43–47], resulting in delocalized states that extend across all leads and exhibit nonlocal Josephson effect [43,48–51]. In Andreev molecules, two primary coherent transport processes occur: double elastic

---

[*] These authors contributed equally to this work.
[†] Contact author: fni@zurich.ibm.com

cotunneling and double crossed Andreev reflection [31,43,52], both essential for the generation of Cooper pair multiplets [31,32,53] and for engineering Kitaev chains [54] in quantum dot arrays [55–65]. Detailed understanding of Andreev band structures in multiterminal devices can be gained through local spectroscopy, which has been employed to probe hybridized ABSs [66,67], as well as spin-split energy levels and ground state parity transitions [68,69]. In these experiments, phase biasing allowed the exploration of ABS spectra as a function of up to two superconducting phase differences [66,69,70]. However, realizing topological phases with nontrivial Chern numbers strictly requires independent tuning of three phase degrees of freedom [21,24,71,72], a challenge that remains to be addressed.

In this work, we realize a 4TJJ where three phases are independently controlled through flux biasing. We probe the ABS energy spectrum of the system across the entire 3D phase space using tunneling spectroscopy. Moreover, we observe the simultaneous hybridization of three ABSs, i.e., the formation of a so-called tri-Andreev molecule, when the three phases are tuned close to π. Our findings are supported by a theoretical model, which qualitatively reproduces the main features of the measured Andreev spectra. Furthermore, our simulations indicate that the Andreev bands undergo a phase-controlled topological transition in which hybridization induces a band inversion accompanied by the appearance of Weyl nodes. Because of the finite resolution of the tunneling spectroscopy, with a linewidth of approximately 15 μeV, the gapless states (Weyl nodes) cannot be experimentally distinguished from the gapped states. Finally, we study the robustness of the topological phase under variations of experimentally addressable parameters, finding that the regime best describing our device is well within the topological region. Overall, our work provides access to Andreev band structures in three synthetic dimensions, creating an experimental platform and practical guidelines for the realization of topological states in hybrid multiterminal devices.

II. EXPERIMENTAL SETUP AND 3D PHASE CONTROL

The device under study, shown in Fig. 1(a), consists of a 4TJJ embedded in a triple-loop geometry. It is realized in an InAs/Al heterostructure [73,74], where the epitaxial Al layer is selectively removed to expose the III–V semiconductor below. Three flux-bias lines are patterned on top of a uniform dielectric layer to generate the external magnetic fluxes Φ_i ($i = L, M, R$) threading the three interconnected superconducting loops (L, M, and R). This enables us to control the phase differences ϕ_i between the four terminals ($T1$–$T4$). The latter couple with a common semiconducting region [see Fig. 1(b)] where a superconducting island with diameter of approximately 90 nm is left at its center to partially screen the probe gate voltages.

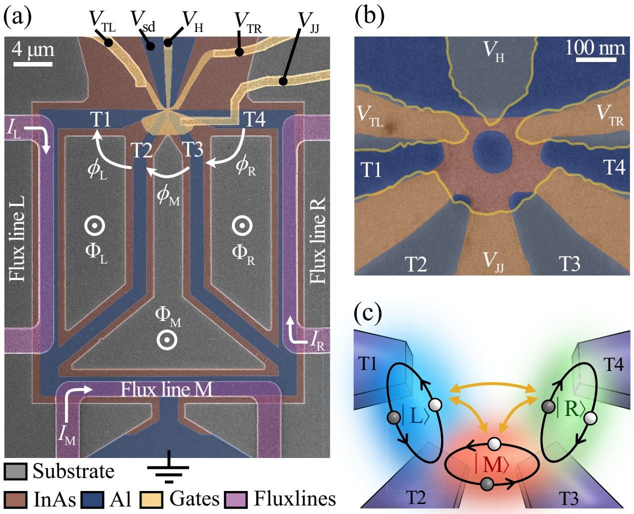

FIG. 1. (a) False-colored scanning electron microscope (SEM) image of a 4TJJ device lithographically identical to that used in the experiment, showing the three-loop geometry. The four superconducting terminals $T1$–$T4$ are labeled, along with the voltage bias V_{sd}, gate voltages V_g ($g \in \{\mathrm{TL}, \mathrm{TR}, \mathrm{H}, \mathrm{JJ}\}$), flux-line currents I_i ($i \in \{L, M, R\}$), magnetic fluxes through the loops Φ_i, and superconducting phase differences ϕ_i across the respective terminal pairs. (b) Enlargement of the four-terminal junction area. The background is an SEM image of a device lithographically identical to that under study, taken prior to gate deposition. The gate structures (yellow) are overlaid by extracting their contours from a second SEM image of an identical device with gates deposited (see Supplemental Material [75] Sec. I for more details). (c) Illustrative representation of the 4TJJ, highlighting its multiterminal character. Three Andreev bound states, labeled $|L\rangle$, $|M\rangle$, and $|R\rangle$, form between terminals $T1$ and $T2$, $T2$ and $T3$, and $T3$ and $T4$, respectively, as indicated by black electron-hole trajectories. Orange arrows represent the couplings between pairs of ABSs. When all three ABSs hybridize, the system is expected to form a tri-Andreev molecule.

By design, the minimum distance between neighboring terminals is 50 nm, while the distance between $T1$ and $T4$ is 220 nm. All these lengths are small in comparison with the superconducting coherence length in the InAs 2DEG, estimated to be 600 nm [49]. Four gate electrodes on the dielectric layer are energized by voltages V_g ($g \in \{\mathrm{TL}, \mathrm{TR}, \mathrm{H}, \mathrm{JJ}\}$), allowing for electrostatic tuning of the electron density in the InAs layer below. Tunneling spectroscopy of the scattering area is performed by measuring the differential conductance G across a tunneling barrier, formed by depleting the InAs region below the gates V_{TL} and V_{TR} (see Supplemental Material [75] Sec. II for additional details). The device was measured in a dilution refrigerator with a base temperature of about 10 mK using lock-in techniques, with a dc voltage bias V_{sd} and an ac voltage bias of amplitude $\delta V_{\mathrm{sd}} = 3$ μV applied between the probe and the four terminals. More information about materials, fabrication, and measurement setup is available in Ref. [66].

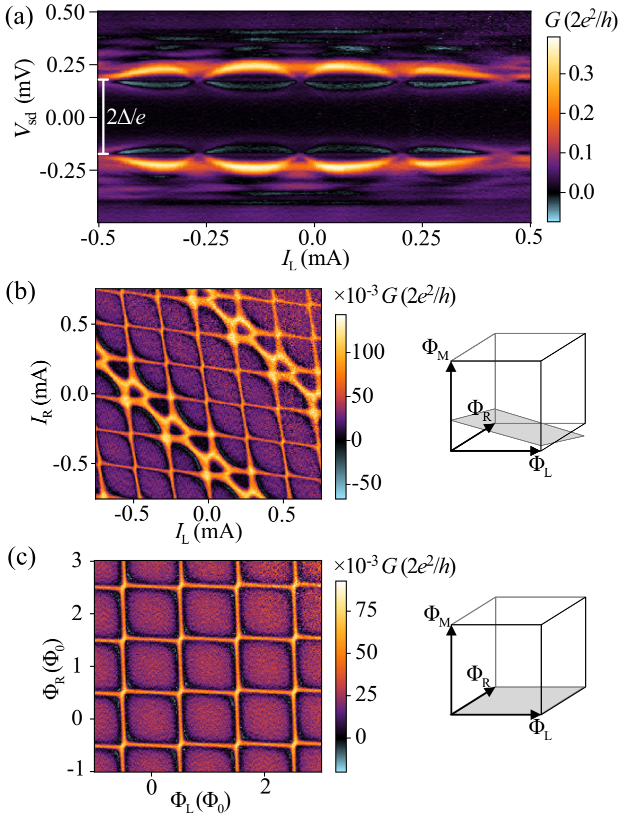

FIG. 2. (a) Tunneling spectroscopy measurement, showing the differential conductance G as a function of voltage bias V_{sd} and the current I_L flowing in flux line L. (b) Differential conductance map measured at $V_{\mathrm{sd}} = -175$ μV as a function of the flux-line currents I_L and I_R. (c) As in (b), but measured as a function of the magnetic fluxes Φ_L and Φ_R after the current-to-flux remapping (see the text). The schematics on the right in (b) and (c) represent the orientations of the corresponding maps with respect to the cubic unit cell in the 3D flux space.

Figure 2(a) shows a typical tunneling spectrum measured by varying the flux-line current I_L and the dc bias V_{sd}. The flux-dependent ABS spectrum is visible outside a transport gap of 350 μV $= 2\Delta/e$, that is due to the superconducting probe (Δ is the superconducting gap). Weaker spectroscopic features are also visible inside the transport gap. Two flux-independent conductance peaks at $V_{\mathrm{sd}} = \pm\Delta/e$ highlight the probe gap edges and are attributed to multiple Andreev reflection processes. Assuming a BCS-like density of states (DOS) for the superconducting probe with peaks at energy $\pm\Delta$, G is expected to have a resonance at a voltage $\pm(\Delta + E)/e$ when a peak is present in the DOS of the scattering area at energy E. Consequently, spectroscopic features observed at $eV_{\mathrm{sd}} = \pm\Delta/e = \pm175$ μeV correspond to DOS peaks at zero energy ($E = 0$) in the scattering area. When half of a superconducting flux quantum ($\Phi_0 = h/2e$) induced by the left flux line penetrates loop L, the superconducting phase difference ϕ_L is tuned to π, and the ABS energy approaches zero energy as for a highly transparent two-terminal JJ [2]. Notably, the dispersion shows an additional modulation with a larger periodicity in I_L, which is evident in the map shown in Fig. 2(b) measured at constant $V_{\mathrm{sd}} = -\Delta/e$ by varying I_L and I_R. Here, we observe a slower modulation along the diagonal direction $I_L = I_R$, caused by the magnetic flux generated by lines L and R impinging through the middle loop. A useful way to navigate within the 3D flux space is to consider the cubic unit cell defined by the three independent magnetic fluxes Φ_L, Φ_M, and Φ_R, as schematically illustrated in the insets in Figs. 2(b) and 2(c). Within this framework, the $I_L - I_R$ map follows a tilted plane sketched in gray, whose orientation is defined by the 3×3 mutual inductance matrix M:

$$\Phi = \begin{pmatrix} \Phi_L \\ \Phi_M \\ \Phi_R \end{pmatrix} = M \begin{pmatrix} I_L \\ I_M \\ I_R \end{pmatrix} + \Phi_{(0,0,0)}, \tag{1}$$

where $\Phi_{(0,0,0)}$ is an offset defining the corner of a unit cell. In order to cut the unit cell in a controlled way, we compensate for the cross-coupling between loops and flux lines by simultaneously setting the three currents I_L, I_M, and I_R needed to reach a flux point Φ, according to Eq. (1). Figure 2(c) shows the differential conductance map measured in this way by sweeping the fluxes Φ_L and Φ_R and keeping $\Phi_M = 0$. As a result, a periodic square net is obtained, demonstrating independent flux control over the three loops. More details about the current-to-flux remapping and how to extract the mutual inductance matrix elements are provided in Ref. [75], Sec. III.

III. ABS ENERGY DISPERSION IN THE 3D FLUX SPACE

Having established a measurement protocol that allows for independent flux control, we systematically map the ABS energy spectrum in the 3D flux space. Owing to the periodicity of the spectrum, we can restrict our investigation to a single 3D flux unit cell. We start with a simple case where we sweep the flux threading a loop while keeping the other two fluxes at zero, as shown in Fig. 3(a) for varying Φ_L. The energy spectrum reveals the dispersion of a highly transparent ABS, that we identify as the mode formed between the terminal pair $T1$ and $T2$. The large transparency (but smaller than 1) is expected to prevent the band from reaching zero energy, forming a minigap between the positive and negative energy branches of the ABS spectrum [3]. However, this small energy gap is not experimentally revolved due to the sizable spectral broadening, estimated to be 15 μeV (see Ref. [75], Sec. IV). Notably, the ABS dispersion does not reach the superconducting gap edge, but it is reduced to $\sim 0.4\Delta/e$, potentially due to the repulsion with the lower-transmission states visible at $V_{\mathrm{sd}} < -0.3$ mV. Figure 3(b) shows the dispersion of the

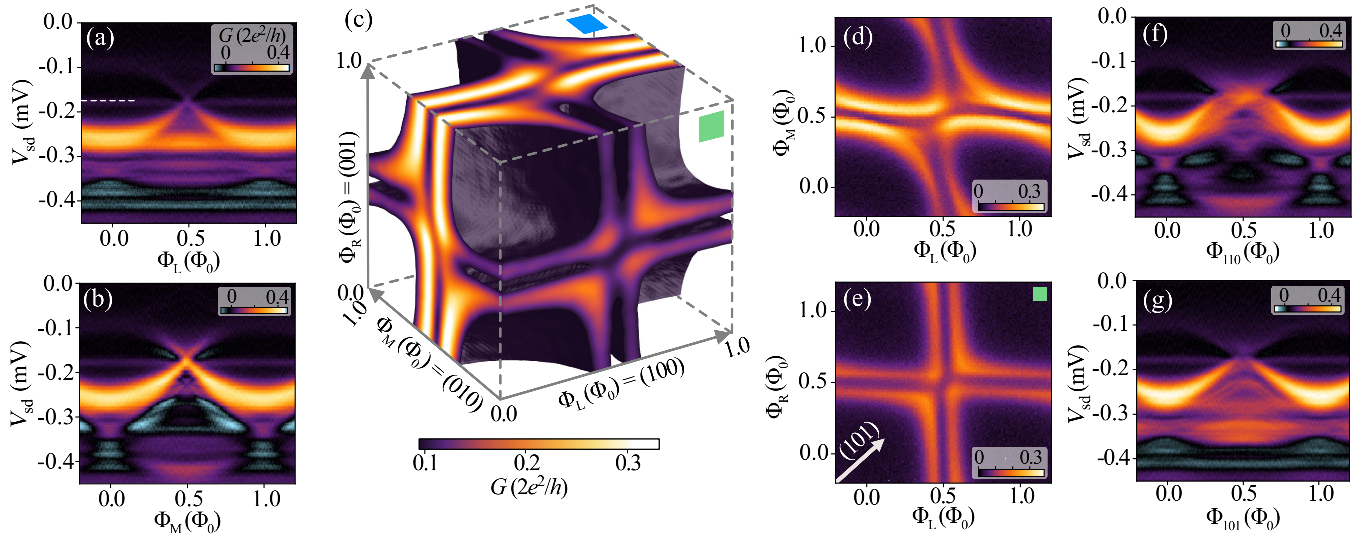

FIG. 3. (a) Tunneling differential conductance G measured as a function of dc voltage bias V_{sd} and magnetic flux Φ_L, with $\Phi_M = \Phi_R = 0$. (b) As in (a), but varying Φ_M with $\Phi_L = \Phi_R = 0$. (c) Tunneling differential conductance measured at fixed $V_{\mathrm{sd}} = -200$ μV and plotted in the 3D flux unit cell for values $G \geq 0.095 \times 2e^2/h$ (the dark purple surfaces represent the isosurfaces of the dataset at this minimum value of differential conductance). The unit cell axes are also labeled using the crystallographiclike notation used to define specific directions in the flux space. (d),(e) Flux-flux maps of two cube faces [as indicated by the colored squares in (c)], measured at $V_{\mathrm{sd}} = -200$ μV, showing avoided crossing induced by the formation of bi-Andreev molecules. (f),(g) G measured as a function of V_{sd} along the directions (110) and (101), as indicated by the white arrows in (d) and (e), respectively.

ABSs formed between $T2$ and $T3$, which are tuned by sweeping Φ_M. Similar to the previous case, the spectrum is dominated by a brighter highly transparent mode having the same reduced dispersion and a low-transmission manifold of states at lower energies. The dispersion of the modes formed between $T3$ and $T4$ (shown in Ref. [75], Sec. IV) is qualitatively equivalent to the one along Φ_L. In the following, we focus on the three high-transmission ABSs that we label $|L\rangle$, $|M\rangle$, and $|R\rangle$ as shown in Fig. 1(c).

To have an overview on how such states disperse in the flux space, we map the differential conductance G fixed at $V_{\mathrm{sd}} = -\Delta/e - 25$ μV within the whole 3D unit cell. In Fig. 3(c), we plot G for values larger than $0.095 \times 2e^2/h$, i.e., where the DOS is nonzero. At this V_{sd} value, the Andreev dispersions are cut twice around $\Phi_i = 0.5\Phi_0$, forming pairs of parallel conductance lines along the cube faces. At the center of each face, the ABSs do not cross each other, but they rather interact opening avoided crossings, as highlighted in the face maps in Figs. 3(d) and 3(e). These avoided crossings are spectral signatures characteristic of bi-Andreev molecular states formed by the hybridization of two ABSs, which have recently been observed in three-terminal devices [66]. Notably, the four-terminal device presented here acts as an effective three-terminal system on the cube faces, i.e., when one flux is kept fixed to zero.

To better define directions in the 3D flux space, we introduce a crystallographiclike notation, where the three flux axes (Φ_L, Φ_M, and Φ_R) are denoted as (100), (010), and (001), respectively. The hybridization lifts the degeneracy of the original two-terminal ABSs, splitting the dispersion in two bands as observed in the spectra in Figs. 3(f) and 3(g), measured along the directions (110) and (101) [white arrows in Figs. 3(d) and 3(e), respectively]. A larger splitting is observed along the (110) direction (f) compared to (101) cut (g), indicating a stronger coupling between the nearest neighbor ABSs $|L\rangle$ and $|M\rangle$. A weaker hybridization is instead expected between $|L\rangle$ and $|R\rangle$, due to their smaller wave function overlap. In Fig. S4 [75], additional tunneling spectra show that the energy splitting is much smaller along the perpendicular directions $\Phi_{10\bar{1}}$ and $\Phi_{1\bar{1}0}$, as expected when the interacting ABSs have opposite phases [43,47,66]. Thus, our observations reveal a significant hybridization between all three ABSs, which couple in pairs to form bi-Andreev molecules on each face of the cubic unit cell.

IV. EXPLORING THE CENTER OF THE UNIT CELL

The device configurations discussed so far reproduce the behavior of either two-terminal devices (when two phase differences are kept to zero, i.e., along the unit cell edges) or three-terminal ones (along the unit cell faces, where only one phase difference is kept to zero). Inside the unit cell, all the phase differences are nonzero, leading to a more complex ABS spectrum achievable only with four or more leads. To explore such configurations, we slice the cubic cell from the $\Phi_L - \Phi_R$ face to the center along parallel planes measured at different Φ_M values and at $V_{\mathrm{sd}} = -\Delta/e$, as shown in Fig. 4(a). At this V_{sd} value, we probe the

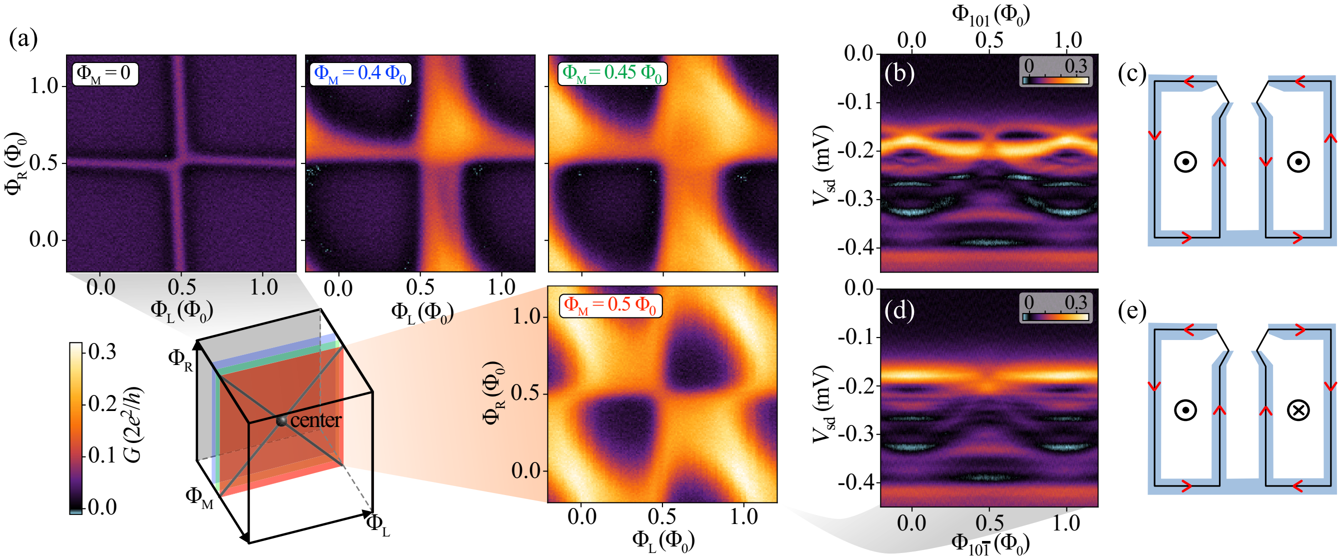

FIG. 4. (a) Slicing the cubic unit cell (see schematic) by measuring Φ_L-Φ_R maps at different values of Φ_M, with voltage bias V_{sd} kept fixed at $-175\ \mu\text{V}$. (b),(c) Cuts measured as a function of V_{sd} along the (101) and $(10\bar{1})$ direction [see gray arrows in (a) at $\Phi_M = 0.5\Phi_0$]. In the schematics on the right in the plots, the currents flowing in the two outer loops of device are sketched, revealing that mutual inductive effects on the center loop are expected along Φ_{101} and not along $\Phi_{10\bar{1}}$.

energy spectrum near the maxima of the ABSs, resulting in one conductance line per state. By increasing Φ_M, the conductance becomes asymmetric around the center of the plot and develops a maximum at $\Phi_L = \Phi_R = 0.7\Phi_0$. Moving Φ_M further to $0.5\Phi_0$, the map recovers its inversion symmetry, featuring two lobes of low conductance around the center. In this configuration, one would expect to measure constant conductance across the entire plane, since $|M\rangle$ is fixed at its energy maximum. Instead, the energy cut along Φ_{101} [Fig. 4(b)] reveals that the state $|M\rangle$ has a relatively weak dispersion just below $V_{\text{sd}} = -0.175$ mV.

We explain the weak influence of $\Phi_{L,R}$ on this ABSs in terms of mutual inductive coupling between loops. When Φ_L and Φ_R are swept in phase (Φ_{101}), two opposite currents flow along the two long sides of loop M, as shown in Fig. 4(c). These currents induce two parallel flux contributions to Φ_M, providing an additional phase difference between $T2$ and $T3$. When Φ_L and Φ_R are swept with opposite sign, i.e., along $\Phi_{10\bar{1}}$, the two currents flow in the same direction as sketched in Fig. 4(e), and the two induced fluxes cancel each other out. Indeed, the spectrum measured along this direction [Fig. 4(d)] shows that $|M\rangle$ forms a flat band independent of the other two fluxes just below $V_{\text{sd}} = -0.175$ mV.

In Fig. 4(d), we also observe two dispersive bands representing the $|L\rangle - |R\rangle$ hybridized states and having their maxima at $\Phi_{10\bar{1}} \sim 0.5\Phi_0$. Here, they interact with the $|M\rangle$-derived flat band which significantly decreases its energy to $V_{\text{sd}} \sim -0.2$ mV. This indicates that an additional gap between the positive and negative energy branches of the overall ABS spectrum is opened in addition to the minigap formed by the finite junction transparency. In the following, we show that this spectral feature marks the hybridization among three two-terminal ABSs occurring when they are tuned to the same energy, i.e., the formation of a tri-Andreev molecule.

V. THEORETICAL MODEL

To better understand how the hybridization between ABSs reshapes the complex Andreev band structure observed in the previous paragraph, we develop a theoretical model schematically represented in Fig. 5(a). The model features four superconducting leads coupled to a normal scattering region described by means of three coupled conduction channels. The superconducting phase differences $\phi_{L,M,R}$ (or, equivalently, magnetic fluxes $\Phi_{L,M,R} = \Phi_0\phi_{L,M,R}/2\pi$) are defined between the leads using the same convention introduced in Fig. 1(a). Each channel contains two noninteracting spin-degenerate levels with on-site energy $\epsilon_i^{\pm}$ ($i = 1, 2, 3$) and is coupled to the neighboring leads with a coupling strength characterized by the parameter Γ, as well as to the other channels, described by the parameter t. All channel-lead couplings and interchannel couplings are assumed to be equal. We note that the choice of a conduction channel network provides a convenient description of a normal region hosting discrete ABSs, with the degree of hybridization among them determined by t. This model is not intended to represent quantum dots with Coulomb interactions but rather to provide a minimal framework to qualitatively describe hybridization effects among ABSs. Coulomb interactions are not included in the model because the normal region is strongly coupled to the leads, resulting in negligible

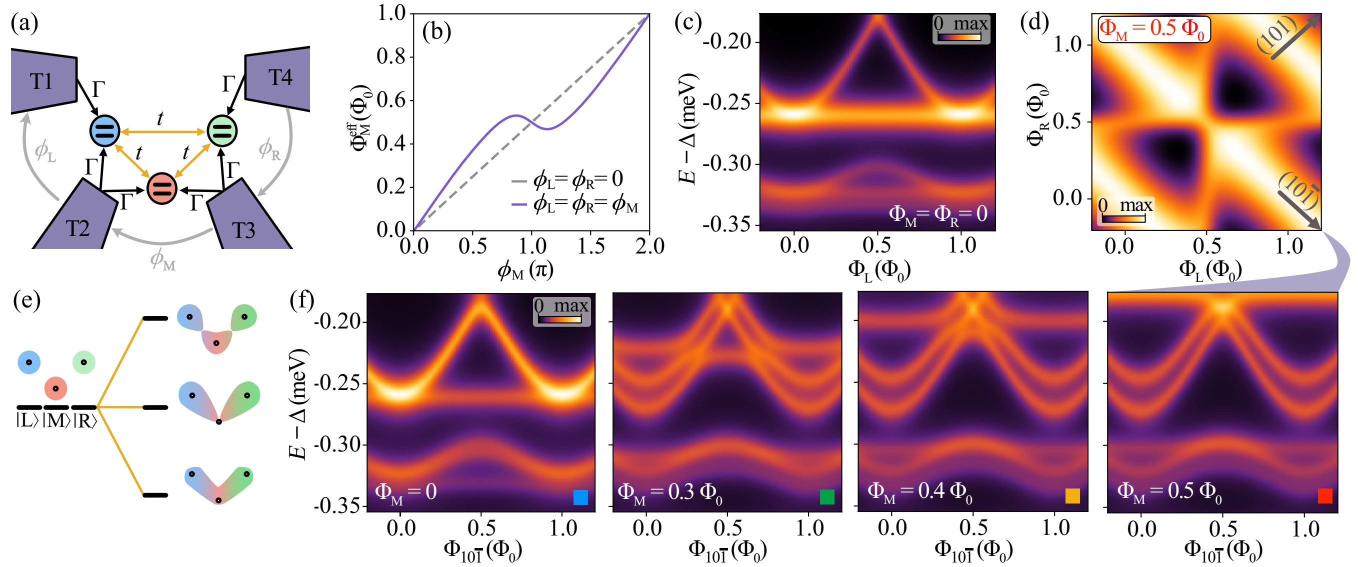

FIG. 5. (a) Schematic of the model comprising three two-level conduction channels (blue, red, and green) coupled to each other and to four superconducting terminals ($T1$–$T4$). ABSs form in the conduction channels and have energies dispersing as a function of the superconducting phase differences ϕ_i. The model parameters (see definitions in the text) are $\epsilon = 0.005\Delta$, $\Gamma = 0.37\Delta$, and $t = 0.12\Delta$. (b) Phase-effective flux relation including mutual inductive coupling between the loops when the other phases ϕ_L and ϕ_R are kept constant to zero (dashed gray line) and when they are equal to ϕ_M (solid purple line). (c) Simulated energy spectrum along Φ_L, with $\Phi_M = \Phi_R = 0$. The energy axis E is shifted by $\Delta = 175$ μeV to align to the experimental data. (d) Simulated flux-flux map at $E = 0$ corresponding to the measurement shown in Fig. 4(a) for $\Phi_M = 0.5\Phi_0$. (e) Conceptual illustration of the hybridization among three degenerate energy levels resulting in bonding, nonbonding, and antibonding states separated by energy gaps, as in a triatomic molecule. (f) Simulated energy spectra along $\Phi_{10\bar{1}}$ for different Φ_M values, showing that hybridization between ABSs opens energy gaps at the crossing points between different levels. The colored squares refer to the arrows in Fig. 6(f).

charging energies, and our experimental data do not show signatures of interaction effects such as Kondo physics or parity transitions. Nevertheless, residual interactions may influence the ABS spectra. A fully interacting treatment (e.g., via numerical renormalization group methods) would be necessary to capture these effects. However, to our knowledge, these methods have not yet been extended to address multiterminal junctions with the complexity of our system, and developing such an approach would require substantial theoretical work beyond the scope of this study.

To compare with the experimental data, we compute the total DOS projected onto the three channels as a function of the energy E and the three superconducting phase differences $\phi_{L,M,R}$ (fluxes $\Phi_{L,M,R}$), indicated in Fig. 5(a). Furthermore, to include the effect of the mutual inductive coupling between the superconducting loops, which causes a nonlinear cross dependence between the phases (magnetic fluxes), we remap them to effective phases $\phi_i^{\rm eff}$ (effective magnetic fluxes $\Phi_i^{\rm eff}$) using the relations

$$\phi^{\rm eff}_{L,R} = \phi_{L,R} + \alpha f(\phi_M),$$

$$\phi^{\rm eff}_{M} = \phi_M + \alpha[f(\phi_L) + f(\phi_R)],$$

where $\phi_i^{\rm eff}/2\pi = \Phi_i^{\rm eff}/\Phi_0$ for $i = L, M, R$. Here, $f(\phi) = -2\partial_\phi[1 - \tau\sin^2(\phi/2)]^{-1/2}$, $\alpha = 0.2$ is the strength of the mutual coupling, and $\tau = 0.9$ introduces nonsinusoidal character to $f(\phi)$. Additional details on the model are discussed in Ref. [75], Secs. VII and VIII. Figure 5(b) illustrates the influence of $\phi_{L,R}$ on $\Phi_M^{\rm eff}(\phi_M)$ as a consequence of the mutual coupling, highlighting a nonlinear behavior when $\phi_{L,R}$ are varied together with ϕ_M.

The simulated DOS as a function of energy and of Φ_L while $\Phi_M = \Phi_R = 0$ is shown in Fig. 5(c). The two energy levels in each of the three channels give rise to two distinct manifolds comprising three modes each. As expected, only one state per manifold has a significant energy dispersion, while the others remain mostly constant in energy. Similar to the tunneling spectra in Figs. 3(a) and 3(b), the simulated band structure exhibits one resonance that approaches $E = 0$ at $\Phi_L = 0.5\Phi_0$, forming a cusp consistent with an isolated high-transmission ABS. Figure 5(d) displays the simulated $\Phi_L - \Phi_R$ plane for constant flux $\Phi_M = 0.5\Phi_0$ and constant energy $E = 0$, which corresponds to the measurement shown in Fig. 4(a). The presence of two lobes of minimum DOS around $\Phi_L = \Phi_R = 0.5\Phi_0$ is captured by the model as a result of the nonlinear cross dependence between the phases, closely mimicking the experimental data.

To focus on the effects of ABS hybridization, we consider the $\Phi_{10\bar{1}}$ direction (in which mutual inductance effects are negligible) and simulate the Andreev spectra as a function of E for different values of Φ_M [Fig. 5(f)]. At $\Phi_M = 0$, $|M\rangle$ remains flat at high energy, while both $|R\rangle$ and $|L\rangle$ form dispersing bands which are nearly degenerate in energy. By increasing Φ_M, the flat state approaches zero energy and forms avoided crossings with the dispersing states. These three nondegenerate ABSs resemble the energy levels of a triatomic molecule, where three molecular orbitals (bonding, nonbonding, and antibonding) are split in energy, as conceptually depicted in Fig. 5(e). At $\Phi_M = 0.5\Phi_0$, the state $|M\rangle$ reaches the energy closest to zero and remains constant around that energy. Here, its dispersion bends downward from zero energy as observed in the corresponding measurement in Fig. 4(c). These results support the interpretation that our device hosts three ABSs hybridizing among each other, forming a tri-Andreev molecule delocalized over the four superconducting terminals.

VI. TRI-ANDREEV MOLECULE

Supported by our theoretical model, we investigate more complex spectral features measured along the diagonals of the cubic unit cell, when all three fluxes are varied. Figure 6(a) shows a map measured at $V_{\mathrm{sd}} = -\Delta/e$ along the $\Phi_{101} - \Phi_M$ plane sketched in the schematic on the left. As previously discussed in Sec. III, $|L\rangle$ and $|R\rangle$ are already hybridized along the Φ_{101} direction, as also visible by the splitting of the conductance line at $\Phi_M = 0$ and $\Phi_{101} = 0.5\Phi_0$. When Φ_M is tuned to $0.5\Phi_0$, these hybridized states mix with $|M\rangle$, forming an avoided crossing which is well reproduced by the simulation displayed in Fig. 6(b). Taking an energy cut along the (1, 1, 1) direction [gray arrow in Fig. 6(a)], we observe how the energy spectrum is affected by the hybridization, as shown in Fig. 6(c). Here, the bands split in energy forming an M-shaped dispersion close to zero energy. Notably, such effect is much stronger compared to the one observed for the bi-Andreev molecules in Figs. 3(f) and 3(g). By simulating the same energy spectrum [Fig. 6(d)], we reproduce a similar M shape of the topmost band and reveal the energy splitting between the three bands representing the bonding, nonbonding, and antibonding molecular states illustrated in Fig. 5(e).

As discussed in Sec. III for the bi-Andreev molecules, the energy splitting induced by the hybridization is strongly anisotropic in the phase space. Figure 6(e) shows the conductance map along the $\Phi_{10\bar{1}} - \Phi_M$ plane sketched in the schematic on the left. Here, the dispersions of $|L\rangle$ and $|R\rangle$ overlap with each other at $\Phi_M = 0$ but split when Φ_M is swept toward $0.5\Phi_0$. Notably, the splitting appears larger along the $(11\bar{1})$ direction compared to $(1\bar{1}\bar{1})$, since $|L\rangle$ has a slightly larger transparency than $|R\rangle$ (see Ref. [75], Sec. VI). Also, the horizontal conductance resonance representing the maximum of $|M\rangle$ significantly decreases in intensity approaching the center of the map. The simulation in Fig. 6(f) reproduces the opening of a low-conductance region at the crossing point, which ultimately derives from the splitting at $E = 0$ observed in the simulated energy spectra in Fig. 5(f). Indeed, those dispersions represent horizontal energy-dependent cuts in Fig. 6(f), at Φ_M values indicated by the colored arrows. Taking an energy-dependent cut along the direction $(1\bar{1}\bar{1})$ [Fig. 6(g)], we observe a sizable splitting into two bands but

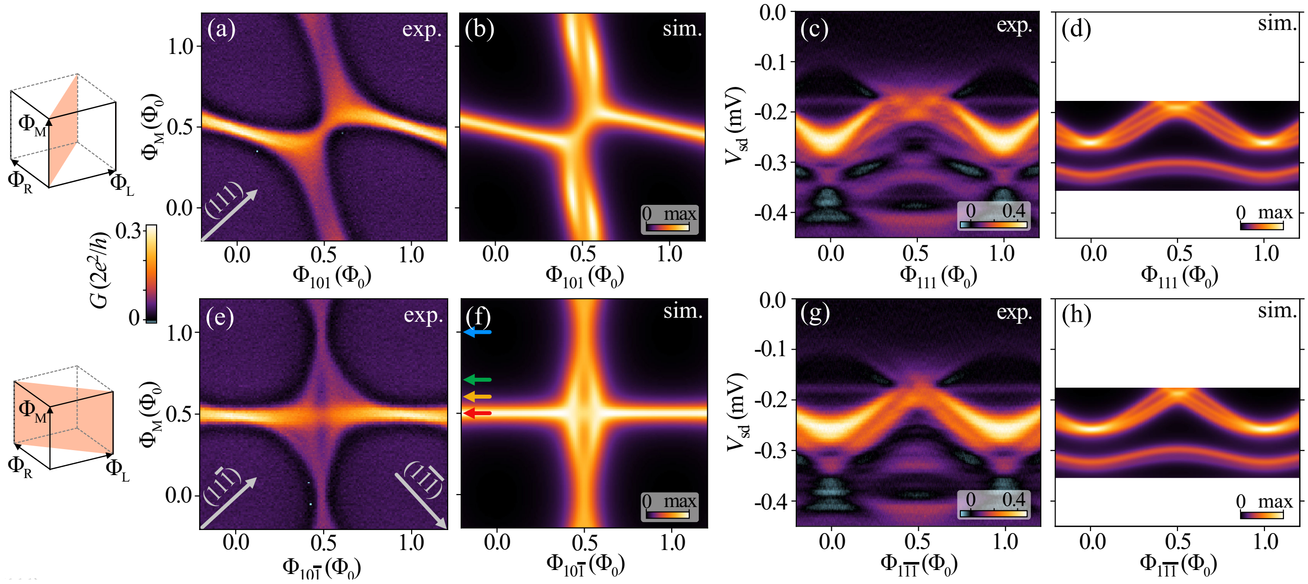

FIG. 6. Experimental (a) and simulated (b) zero-energy plane (at fixed $V_{\mathrm{sd}} = -175$ μV or $E = 0$, respectively) along a diagonal of the cubic unit cell (top-left schematic). Experimental (c) and simulated (d) energy spectrum along the diagonal direction of (a) and (b), i.e., along the flux direction Φ_{111} [gray arrow in (a)]. (e),(f) As in (a),(b), but along another diagonal plane of the cubic unit cell $\Phi_{10\bar{1}} - \Phi_M$ (bottom-left schematic). Experimental (g) and simulated (h) energy spectrum along the flux direction $\Phi_{1\bar{1}\bar{1}}$ [gray arrow in (e)].

smaller than the splitting observed along the (111) direction. The overall hybridization strength is indeed reduced along the direction $(1\bar{1}\bar{1})$, since two phases always have opposite values. Therefore, two bands are expected to remain nearly degenerate, as reproduced in the simulated spectrum in Fig. 6(h).

In summary, the dispersion of a tri-Andreev molecule is characterized by an anisotropic energy splitting, larger along the (111) direction and weaker along its perpendicular direction $(1\bar{1}\bar{1})$. This is directly reflected into the different shapes of the avoided crossings observed at the center of the cube diagonal conductance maps in Figs. 6(a) and 6(e). The spectral signatures of a tri-Andreev molecule discussed here are also observed in a second device (see Ref. [75], Sec. IX).

VII. TOPOLOGICAL ANDREEV BANDS

The hybridization between the three ABSs in our device leads to the formation of molecularlike states whose energy depends on all three superconducting phase differences. This property is one of the requirements for the formation of Weyl nodes, which would appear as zero-energy crossing points with linear dispersion as a function of all the three phases. In the following, we analyze the simulated Andreev band structure matching our experimental results. In Fig. 7(a), we show the ABSs spectrum extracted from the maxima of the density of states for $\phi_M = 0.21\pi$. Here, the two particle-hole symmetric bands closest to the Fermi level form a zero-energy crossing at $\phi_L = \phi_R = 0.89\pi$ as highlighted in the enlarged plot in Fig. 7(b). Increasing ϕ_M, we obtain gapped states [see Fig. 7(c)] with a small energy gap. The gap is closed again at $\phi_M = 0.96\pi$, where another zero-energy crossing appears at $\phi_L \sim \phi_R \sim 0.6\pi$ [Fig. 7(d)]. Within the whole cubic unit cell, we find four zero-energy crossings appearing in two pairs [red and blue points in Fig. 7(e)], which are related by time-reversal symmetry.

As shown in Refs. [76–78], the full information about the topology of the ABS spectrum is encoded in the topological Hamiltonian H_{top}, given by the inverse of the central Green's functions G_{C} evaluated at zero energy, i.e., $H_{\mathrm{top}} = -G_{\mathrm{C}}^{-1}(E=0)$. H_{top} depends on the dimensionless parameters $\tilde{\epsilon} = \epsilon/\Gamma$ and $\tilde{t} = t/\Gamma$ [24,27] (see more details in Ref. [75], Sec. VIII). The values of t and ϵ used for the DOS simulations matching our measurements correspond to $\tilde{\epsilon} \approx 0.01$ and $\tilde{t} \approx 0.32$. By diagonalizing H_{top}, we obtain the eigenvectors $|v_i\rangle$ and the corresponding spin-degenerate eigenenergies. To establish the topological properties of the ABSs, we compute the topological invariant following the numerical method in Ref. [79]. The Chern number is given by

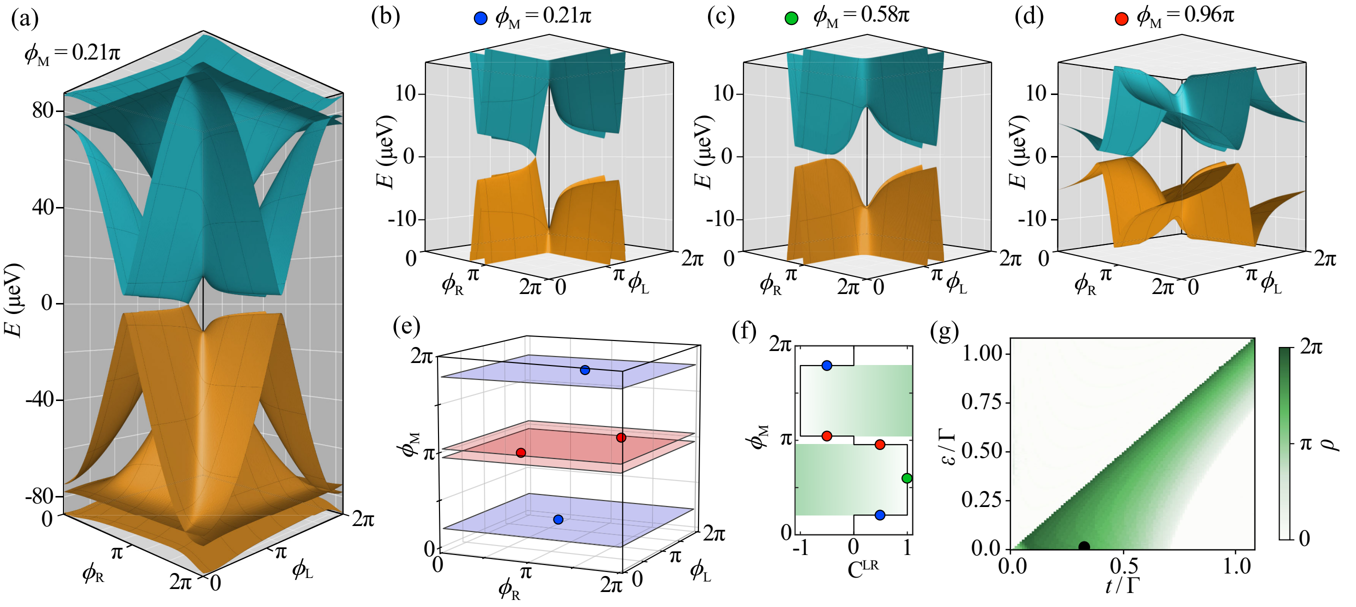

FIG. 7. (a) ABS spectra extracted from the density of states as a function of the phase differences ϕ_L and ϕ_R for fixed $\phi_M = 0.21\pi$. The energy gap between the highest band with $E < 0$ and the lowest band with $E > 0$ vanishes in one point, where a Weyl node forms. (b) Enlargement of (a) around zero energy, highlighting the Weyl node. (c) As in (b), but for $\phi_M = 0.58\pi$. A topological gap is present between the bands. (d) As in (b), but for $\phi_M = 0.96\pi$, showing a second Weyl node with opposite topological charge where the gap closes. The parameters are the same as in Figs. 5 and 6. (e) Positions of the positively (blue) and negatively (red) charged Weyl nodes in the 3D phase space. (f) Chern number C^{LR} calculated as a function of ϕ_M with $\tilde{\epsilon} \approx 0.01$ and $\tilde{t} \approx 0.32$, showing extensive topologically nontrivial regions where $|C^{LR}| = 1$ (green shading). (g) Topological phase diagram displaying the ϕ_M range of the topological region, ρ, as a function of the model parameters $\tilde{\epsilon}$ and $\tilde{t}$. The diagram shows the robustness of the topological phase that is present for $\rho > 0$. The black dot indicates the parametric point corresponding to the model used in Figs. 5 and 6.

$$C_i^{LR}(\phi_M) = \frac{1}{2\pi}\int_0^{2\pi}\int_0^{2\pi} B_i^{LR}(\phi_L,\phi_R,\phi_M)\,d\phi_L d\phi_R, \qquad (2)$$

with the total Chern number $C^{LR} = \sum_{i=1,2,3} C_i^{LR}$ as the sum over all occupied bands and $B_i^{LR} \equiv -2\,\mathrm{Im}\langle\partial_{\phi_L} v_i|\partial_{\phi_R} v_i\rangle$ represents the Berry curvature calculated at fixed ϕ_M. Figure 7(f) shows two distinct nontrivial topological phases having a Chern number equal to ±1 within extensive ϕ_M intervals indicated by the green areas. Therefore, the zero-energy crossing points in Fig. 7(e) are positively (blue) and negatively (red) charged Weyl nodes appearing in the energy spectra [Figs. 7(b) and 7(d)] as the states cross the Fermi level. The eigenenergies of the topological Hamiltonian for the same parameters as in Fig. 7 are shown in Fig. S7 [75]. The eigenenergies exhibit zero-energy states exactly when one local maximum of the DOS is at zero energy, as expected. Notably, the spectrum shown in Fig. 7(c) represents a topological insulating phase with a small energy gap. Since such features are masked by the relatively large spectral broadening in our measurements, we cannot experimentally confirm the predicted topological phase transitions.

To evaluate the robustness of the topological regime in our simulations, we calculate the extension ρ of the region in ϕ_M where the Chern number differs from zero [green areas in Fig. 7(f)] as a function of the two key parameters of our model, $\tilde{\epsilon}$ and $\tilde{t}$. The phase diagram in Fig. 7(g) shows a first topological transition when the hybridization $\tilde{t}$ exceeds $\tilde{\epsilon}$. Intuitively, the hybridization has to be large enough to push one state through zero energy, a mechanism analogous to the band inversion driven by spin-orbit coupling occurring in topological insulators [80]. By further increasing $\tilde{t}$, the two opposite charged Weyl nodes get closer to each other, gradually reducing ρ to zero. At this point, the oppositely charged Weyl nodes annihilate with each other, completely suppressing the topological phase. The parameters used for simulating our measurements corresponds to $\tilde{\epsilon} = 0.01$ and $\tilde{t} = 0.32$, which places our system well within the calculated topological region as indicated by the black dot in Fig. 7(g).

VIII. DISCUSSION AND CONCLUSIONS

In this work, we studied the hybridization between ABSs in a 4TJJ and demonstrated the formation of a tri-Andreev molecule. This state, whose energy is controlled by three superconducting phase differences, is expected to support topological Andreev bands. According to our model, Weyl nodes emerge when the hybridization shifts at least one ABS through zero energy, inducing an inversion between positive and negative energy bands in certain regions of the phase space. By varying ϕ_M, the system undergoes four topological transitions marked by Weyl nodes as shown in Fig. 7(f). The Andreev bands as a function of ϕ_L-ϕ_R have an energy gap ranging between 0 (at the Weyl nodes) and approximately 7 μeV, depending on ϕ_M. The resolution of tunneling spectroscopy, approximately 15 μeV, prevents us from experimentally resolving any gapped states in the low-energy spectrum. Thus, the spectral detection of Weyl nodes would be facilitated by a larger minigap, which could be obtained through an increase of the superconducting gap Δ or by an enhanced device tunability. For example, a larger minigap would be obtained by making the coupling parameters [see Γ in Fig. 5(a)] asymmetric or by increasing ϵ while keeping a sufficiently large hybridization strength. The phase diagram shown in Fig. 7(g) provides a useful guideline for engineering these parameters while preserving the topological properties of the device.

Advanced spectroscopic techniques, such as nonlocal spectroscopy [81,82] and spectroscopy via quantum dots [83,84], might be beneficial for detecting the gap closing and reopening, expected at the Weyl nodes, and for increasing the spectroscopic resolution, respectively. A direct signature of topological transitions would require measuring the quantized transconductance induced by the Chern number variation as a function of Φ_M [21]. However, a voltage-biased device would require splitting the triple loop geometry and, hence, losing the phase control, which is essential for accessing the full energy spectrum.

The large transparency and hybridization strength observed in our 4TJJ already fall well into the stability range of the topological state. Experimental techniques with higher energy resolution would be highly favorable for confirming the presence of Weyl nodes in the ABS spectrum, even in systems with such a large transparency. Microwave spectroscopy, in particular, offers sub-μV resolution, making it well suited for this purpose. Furthermore, hybrid InAs/Al heterostructures are readily integrated in circuit QED architectures [11,14,85–88], offering a tangible prospect for studies of topological Andreev band structure. The employment of polarized microwave radiation can also make this technique sensitive to the Berry curvature [24].

In summary, we realized a phase-controlled 4TJJ and studied its energy spectrum using tunneling spectroscopy. The measurement protocol based on independent flux control developed here allows the systematic exploration of the Andreev spectrum in the 3D phase space. We identified the spectral signatures of a tri-Andreev molecule resulting from the simultaneous hybridization of three ABSs. A numerical model reproduced the key experimental observation and suggested that the current generation of devices already hosts topological Andreev bands. In the light of our results, phase-tunable MTJJs offer new opportunities for studying topological phases in high-dimensional synthetic band structures and developing novel superconducting quantum circuits [89].

ACKNOWLEDGMENTS

We thank Manuel Hinderling for useful discussions. We thank the Cleanroom Operations Team of the Binnig and Rohrer Nanotechnology Center (BRNC) for their help and support. D. C. O., A. E. S., and W. B. acknowledge support by the Deutsche Forschungsgemeinschaft (DFG; German Research Foundation) via SFB 1432 (Project No. 425217212) and Project No. 467596333 and by the Excellence Strategy of the University of Konstanz via a Blue Sky project. J. C. C. thanks the Spanish Ministry of Science and Innovation (Grant No. PID2020–114880 GB-I00) for financial support and the DFG and SFB 1432 for sponsoring his stay at the University of Konstanz as a Mercator Fellow. W. W. acknowledges support from the Swiss National Science Foundation (Grant No. 200020_207538). F. N. acknowledges support from the European Research Council (Grant No. 804273) and the Swiss National Science Foundation (Grant No. 200021_201082).

DATA AVAILABILITY

The data that support the findings of this article are openly available [90].

[1] A. F. Andreev, *Thermal conductivity of the intermediate state of superconductors*, Sov. Phys. JETP **19**, 1228 (1964).

[2] C. W. J. Beenakker and H. van Houten, *Josephson current through a superconducting quantum point contact shorter than the coherence length*, Phys. Rev. Lett. **66**, 3056 (1991).

[3] C. W. J. Beenakker, *Universal limit of critical-current fluctuations in mesoscopic Josephson junctions*, Phys. Rev. Lett. **67**, 3836 (1991).

[4] A. Furusaki and M. Tsukada, *Current-carrying states in Josephson junctions*, Phys. Rev. B **43**, 10164 (1991).

[5] J.-D. Pillet, C. H. L. Quay, P. Morfin, C. Bena, A. L. Yeyati, and P. Joyez, *Andreev bound states in supercurrent-carrying carbon nanotubes revealed*, Nat. Phys. **6**, 965 (2010).

[6] L. Bretheau, Ç. Ö. Girit, H. Pothier, D. Esteve, and C. Urbina, *Exciting Andreev pairs in a superconducting atomic contact*, Nature (London) **499**, 312 (2013).

[7] L. Bretheau, Ç. Ö. Girit, C. Urbina, D. Esteve, and H. Pothier, *Supercurrent spectroscopy of Andreev states*, Phys. Rev. X **3**, 041034 (2013).

[8] E. J. H. Lee, X. Jiang, M. Houzet, R. Aguado, C. M. Lieber, and S. D. Franceschi, *Spin-resolved Andreev levels and parity crossings in hybrid superconductor–semiconductor nanostructures*, Nat. Nanotechnol. **9**, 79 (2014).

[9] D. J. van Woerkom, A. Proutski, B. van Heck, D. Bouman, J. I. Väyrynen, L. I. Glazman, P. Krogstrup, J. Nygård, L. P. Kouwenhoven, and A. Geresdi, *Microwave spectroscopy of spinful Andreev bound states in ballistic semiconductor Josephson junctions*, Nat. Phys. **13**, 876 (2017).

[10] M. Hays, V. Fatemi, K. Serniak, D. Bouman, S. Diamond, G. de Lange, P. Krogstrup, J. Nygård, A. Geresdi, and M. H. Devoret, *Continuous monitoring of a trapped superconducting spin*, Nat. Phys. **16**, 1103 (2020).

[11] L. Tosi, C. Metzger, M. F. Goffman, C. Urbina, H. Pothier, S. Park, A. L. Yeyati, J. Nygård, and P. Krogstrup, *Spin-orbit splitting of Andreev states revealed by microwave spectroscopy*, Phys. Rev. X **9**, 011010 (2019).

[12] F. Nichele, E. Portolés, A. Fornieri, A. M. Whiticar, A. C. C. Drachmann, S. Gronin, T. Wang, G. C. Gardner, C. Thomas, A. T. Hatke, M. J. Manfra, and C. M. Marcus, *Relating Andreev bound states and supercurrents in hybrid Josephson junctions*, Phys. Rev. Lett. **124**, 226801 (2020).

[13] C. Janvier, L. Tosi, L. Bretheau, C. O. Girit, M. Stern, P. Bertet, P. Joyez, D. Vion, D. Esteve, M. F. Goffman, H. Pothier, and C. Urbina, *Coherent manipulation of Andreev states in superconducting atomic contacts*, Science **349**, 1199 (2015).

[14] M. Hays, G. de Lange, K. Serniak, D. J. van Woerkom, D. Bouman, P. Krogstrup, J. Nygård, A. Geresdi, and M. H. Devoret, *Direct microwave measurement of Andreev-bound-state dynamics in a semiconductor-nanowire Josephson junction*, Phys. Rev. Lett. **121**, 047001 (2018).

[15] M. Hays, V. Fatemi, D. Bouman, J. Cerrillo, S. Diamond, K. Serniak, T. Connolly, P. Krogstrup, J. Nygård, A. L. Yeyati, A. Geresdi, and M. H. Devoret, *Coherent manipulation of an Andreev spin qubit*, Science **373**, 430 (2021).

[16] M. Pita-Vidal, A. Bargerbos, R. Žitko, L. J. Splitthoff, L. Grünhaupt, J. J. Wesdorp, Y. Liu, L. P. Kouwenhoven, R. Aguado, B. van Heck, A. Kou, and C. K. Andersen, *Direct manipulation of a superconducting spin qubit strongly coupled to a transmon qubit*, Nat. Phys. **19**, 1110 (2023).

[17] V. Mourik, K. Zuo, S. M. Frolov, S. R. Plissard, E. P. A. M. Bakkers, and L. P. Kouwenhoven, *Signatures of Majorana fermions in hybrid superconductor-semiconductor nanowire devices*, Science **336**, 1003 (2012).

[18] F. Nichele, A. C. C. Drachmann, A. M. Whiticar, E. C. T. O'Farrell, H. J. Suominen, A. Fornieri, T. Wang, G. C. Gardner, C. Thomas, A. T. Hatke, P. Krogstrup, M. J. Manfra, K. Flensberg, and C. M. Marcus, *Scaling of Majorana zero-bias conductance peaks*, Phys. Rev. Lett. **119**, 136803 (2017).

[19] A. Fornieri, A. M. Whiticar, F. Setiawan, E. Portolés, A. C. C. Drachmann, A. Keselman, S. Gronin, C. Thomas, T. Wang, R. Kallaher, G. C. Gardner, E. Berg, M. J. Manfra, A. Stern, C. M. Marcus, and F. Nichele, *Evidence of topological superconductivity in planar Josephson junctions*, Nature (London) **569**, 89 (2019).

[20] H. Ren, F. Pientka, S. Hart, A. T. Pierce, M. Kosowsky, L. Lunczer, R. Schlereth, B. Scharf, E. M. Hankiewicz, L. W. Molenkamp, B. I. Halperin, and A. Yacoby, *Topological superconductivity in a phase-controlled Josephson junction*, Nature (London) **569**, 93 (2019).

[21] R.-P. Riwar, M. Houzet, J. S. Meyer, and Y. V. Nazarov, *Multi-terminal Josephson junctions as topological matter*, Nat. Commun. **7**, 11167 (2016).

[22] E. Eriksson, R.-P. Riwar, M. Houzet, J. S. Meyer, and Y. V. Nazarov, *Topological transconductance quantization in a four-terminal Josephson junction*, Phys. Rev. B **95**, 075417 (2017).

[23] H.-Y. Xie, M. G. Vavilov, and A. Levchenko, *Weyl nodes in Andreev spectra of multiterminal Josephson junctions: Chern numbers, conductances, and supercurrents*, Phys. Rev. B **97**, 035443 (2018).

[24] R. L. Klees, G. Rastelli, J. C. Cuevas, and W. Belzig, *Microwave spectroscopy reveals the quantum geometric tensor of topological Josephson matter*, Phys. Rev. Lett. **124**, 197002 (2020).

[25] H.-Y. Xie, J. Hasan, and A. Levchenko, *Non-Abelian monopoles in the multiterminal Josephson effect*, Phys. Rev. B **105**, L241404 (2022).

[26] E. V. Repin and Y. V. Nazarov, *Weyl points in multiterminal hybrid superconductor-semiconductor nanowire devices*, Phys. Rev. B **105**, L041405 (2022).

[27] L. Teshler, H. Weisbrich, J. Sturm, R. L. Klees, G. Rastelli, and W. Belzig, *Ground state topology of a four-terminal superconducting double quantum dot*, SciPost Phys. **15**, 214 (2023).

[28] Y. Chen and Y. V. Nazarov, *Spin Weyl quantum unit: A theoretical proposal*, Phys. Rev. B **103**, 045410 (2021).

[29] V. Boogers, J. Erdmanis, and Y. Nazarov, *Holonomic quantum manipulation in the Weyl disk*, Phys. Rev. B **105**, 235437 (2022).

[30] Y. Chen and Y. V. Nazarov, *Spintronics with a Weyl point in superconducting nanostructures*, Phys. Rev. B **103**, 165424 (2021).

[31] A. Freyn, B. Douçot, D. Feinberg, and R. Mélin, *Production of nonlocal quartets and phase-sensitive entanglement in a superconducting beam splitter*, Phys. Rev. Lett. **106**, 257005 (2011).

[32] T. Jonckheere, J. Rech, T. Martin, B. Douçot, D. Feinberg, and R. Mélin, *Multipair dc Josephson resonances in a biased all-superconducting bijunction*, Phys. Rev. B **87**, 214501 (2013).

[33] A. H. Pfeffer, J. E. Duvauchelle, H. Courtois, R. Mélin, D. Feinberg, and F. Lefloch, *Subgap structure in the conductance of a three-terminal Josephson junction*, Phys. Rev. B **90**, 075401 (2014).

[34] Y. Cohen, Y. Ronen, J.-H. Kang, M. Heiblum, D. Feinberg, R. Mélin, and H. Shtrikman, *Nonlocal supercurrent of quartets in a three-terminal Josephson junction*, Proc. Natl. Acad. Sci. U.S.A. **115**, 6991 (2018).

[35] K.-F. Huang, Y. Ronen, R. Mélin, D. Feinberg, K. Watanabe, T. Taniguchi, and P. Kim, *Evidence for 4e charge of Cooper quartets in a biased multi-terminal graphene-based Josephson junction*, Nat. Commun. **13**, 3032 (2022).

[36] A. W. Draelos, M.-T. Wei, A. Seredinski, H. Li, Y. Mehta, K. Watanabe, T. Taniguchi, I. V. Borzenets, F. Amet, and G. Finkelstein, *Supercurrent flow in multiterminal graphene Josephson junctions*, Nano Lett. **19**, 1039 (2019).

[37] G. V. Graziano, J. S. Lee, M. Pendharkar, C. J. Palmstrøm, and V. S. Pribiag, *Transport studies in a gate-tunable three-terminal Josephson junction*, Phys. Rev. B **101**, 054510 (2020).

[38] N. Pankratova, H. Lee, R. Kuzmin, K. Wickramasinghe, W. Mayer, J. Yuan, M. G. Vavilov, J. Shabani, and V. E. Manucharyan, *Multiterminal Josephson effect*, Phys. Rev. X **10**, 031051 (2020).

[39] E. G. Arnault, T. F. Q. Larson, A. Seredinski, L. Zhao, S. Idris, A. McConnell, K. Watanabe, T. Taniguchi, I. Borzenets, F. Amet, and G. Finkelstein, *Multiterminal inverse AC Josephson effect*, Nano Lett. **21**, 9668 (2021).

[40] G. V. Graziano, M. Gupta, M. Pendharkar, J. T. Dong, C. P. Dempsey, C. Palmstrøm, and V. S. Pribiag, *Selective control of conductance modes in multi-terminal Josephson junctions*, Nat. Commun. **13**, 5933 (2022).

[41] M. Gupta, G. V. Graziano, M. Pendharkar, J. T. Dong, C. P. Dempsey, C. Palmstrøm, and V. S. Pribiag, *Gate-tunable superconducting diode effect in a three-terminal Josephson device*, Nat. Commun. **14**, 3078 (2023).

[42] M. Coraiola, A. E. Svetogorov, D. Z. Haxell, D. Sabonis, M. Hinderling, S. C. ten Kate, E. Cheah, F. Krizek, R. Schott, W. Wegscheider, J. C. Cuevas, W. Belzig, and F. Nichele, *Flux-tunable Josephson diode effect in a hybrid four-terminal Josephson junction*, ACS Nano **18**, 9221 (2024).

[43] J.-D. Pillet, V. Benzoni, J. Griesmar, J.-L. Smirr, and Ç. O. Girit, *Nonlocal Josephson effect in Andreev molecules*, Nano Lett. **19**, 7138 (2019).

[44] V. Kornich, H. S. Barakov, and Y. V. Nazarov, *Fine energy splitting of overlapping Andreev bound states in multiterminal superconducting nanostructures*, Phys. Rev. Res. **1**, 033004 (2019).

[45] A. Keliri and B. Douçot, *Driven Andreev molecule*, Phys. Rev. B **107**, 094505 (2023).

[46] M. Kocsis, Z. Scherübl, G. Fülöp, P. Makk, and S. Csonka, *Strong nonlocal tuning of the current-phase relation of a quantum dot based Andreev molecule*, Phys. Rev. B **109**, 245133 (2024).

[47] P. D. Johannsen and C. Schrade, *Fermionic quantum simulation on Andreev bound state superlattices*, Phys. Rev. Res. **7**, 023153 (2025).

[48] S. Matsuo, J. S. Lee, C.-Y. Chang, Y. Sato, K. Ueda, C. J. Palmstrøm, and S. Tarucha, *Observation of nonlocal Josephson effect on double InAs nanowires*, Commun. Phys. **5**, 221 (2022).

[49] D. Z. Haxell, M. Coraiola, M. Hinderling, S. C. ten Kate, D. Sabonis, A. E. Svetogorov, W. Belzig, E. Cheah, F. Krizek, R. Schott, W. Wegscheider, and F. Nichele, *Demonstration of the nonlocal Josephson effect in Andreev molecules*, Nano Lett. **23**, 7532 (2023).

[50] S. Matsuo, T. Imoto, T. Yokoyama, Y. Sato, T. Lindemann, S. Gronin, G. C. Gardner, M. J. Manfra, and S. Tarucha, *Phase engineering of anomalous Josephson effect derived from Andreev molecules*, Sci. Adv. **9**, eadj369 (2023).

[51] C. G. Prosko, W. D. Huisman, I. Kulesh, D. Xiao, C. Thomas, M. J. Manfra, and S. Goswami, *Flux-tunable Josephson effect in a four-terminal junction*, Phys. Rev. B **110**, 064518 (2024).

[52] G. Deutscher and D. Feinberg, *Coupling superconducting-ferromagnetic point contacts by Andreev reflections*, Appl. Phys. Lett. **76**, 487 (2000).

[53] D. C. Ohnmacht, M. Coraiola, J. J. García-Esteban, D. Sabonis, F. Nichele, W. Belzig, and J. C. Cuevas, *Quartet tomography in multiterminal Josephson junctions*, Phys. Rev. B **109**, L241407 (2024).

[54] A. Y. Kitaev, *Unpaired Majorana fermions in quantum wires*, Phys. Usp. **44**, 131 (2001).

[55] J. D. Sau and S. D. Sarma, *Realizing a robust practical Majorana chain in a quantum-dot-superconductor linear array*, Nat. Commun. **3**, 964 (2012).

[56] M. Leijnse and K. Flensberg, *Parity qubits and poor man's Majorana bound states in double quantum dots*, Phys. Rev. B **86**, 134528 (2012).

[57] I. C. Fulga, A. Haim, A. R. Akhmerov, and Y. Oreg, *Adaptive tuning of Majorana fermions in a quantum dot chain*, New J. Phys. **15**, 045020 (2013).

[58] C.-X. Liu, G. Wang, T. Dvir, and M. Wimmer, *Tunable superconducting coupling of quantum dots via Andreev*

bound states in semiconductor-superconductor nanowires, Phys. Rev. Lett. **129**, 267701 (2022).

[59] G. Wang, T. Dvir, G. P. Mazur, C.-X. Liu, N. van Loo, S. L. D. ten Haaf, A. Bordin, S. Gazibegovic, G. Badawy, E. P. A. M. Bakkers, M. Wimmer, and L. P. Kouwenhoven, *Singlet and triplet Cooper pair splitting in hybrid superconducting nanowires*, Nature (London) **612**, 448 (2022).

[60] A. Bordin, G. Wang, C.-X. Liu, S. L. D. ten Haaf, N. van Loo, G. P. Mazur, D. Xu, D. van Driel, F. Zatelli, S. Gazibegovic, G. Badawy, E. P. A. M. Bakkers, M. Wimmer, L. P. Kouwenhoven, and T. Dvir, *Tunable crossed Andreev reflection and elastic cotunneling in hybrid nanowires*, Phys. Rev. X **13**, 031031 (2023).

[61] A. Bordin, X. Li, D. van Driel, J. C. Wolff, Q. Wang, S. L. D. ten Haaf, G. Wang, N. van Loo, L. P. Kouwenhoven, and T. Dvir, *Crossed Andreev reflection and elastic cotunneling in three quantum dots coupled by superconductors*, Phys. Rev. Lett. **132**, 056602 (2024).

[62] D. van Driel, B. Roovers, F. Zatelli, A. Bordin, G. Wang, N. van Loo, J. C. Wolff, G. P. Mazur, S. Gazibegovic, G. Badawy, E. P. A. M. Bakkers, L. P. Kouwenhoven, and T. Dvir, *Charge sensing the parity of an Andreev molecule*, PRX Quantum **5**, 020301 (2024).

[63] A. Bordin, F. J. B. Evertsz', G. O. Steffensen, T. Dvir, G. P. Mazur, D. van Driel, N. van Loo, J. C. Wolff, E. P. A. M. Bakkers, A. L. Yeyati, and L. P. Kouwenhoven, *Impact of Andreev bound states within the leads of a quantum dot Josephson junction*, Phys. Rev. X **15**, 011046 (2025).

[64] T. Dvir, G. Wang, N. van Loo, C.-X. Liu, G. P. Mazur, A. Bordin, S. L. D. ten Haaf, J.-Y. Wang, D. van Driel, F. Zatelli, X. Li, F. K. Malinowski, S. Gazibegovic, G. Badawy, E. P. A. M. Bakkers, M. Wimmer, and L. P. Kouwenhoven, *Realization of a minimal Kitaev chain in coupled quantum dots*, Nature (London) **614**, 445 (2023).

[65] S. L. D. ten Haaf, Q. Wang, A. M. Bozkurt, C.-X. Liu, I. Kulesh, P. Kim, D. Xiao, C. Thomas, M. J. Manfra, T. Dvir, M. Wimmer, and S. Goswami, *A two-site Kitaev chain in a two-dimensional electron gas*, Nature (London) **630**, 329 (2024).

[66] M. Coraiola, D. Z. Haxell, D. Sabonis, H. Weisbrich, A. E. Svetogorov, M. Hinderling, S. C. ten Kate, E. Cheah, F. Krizek, R. Schott, W. Wegscheider, J. C. Cuevas, W. Belzig, and F. Nichele, *Phase-engineering the Andreev band structure of a three-terminal Josephson junction*, Nat. Commun. **14**, 6784 (2023).

[67] S. Matsuo, T. Imoto, T. Yokoyama, Y. Sato, T. Lindemann, S. Gronin, G. C. Gardner, S. Nakosai, Y. Tanaka, M. J. Manfra, and S. Tarucha, *Phase-dependent Andreev molecules and superconducting gap closing in coherently-coupled Josephson junctions*, Nat. Commun. **14**, 8271 (2023).

[68] B. van Heck, S. Mi, and A. R. Akhmerov, *Single fermion manipulation via superconducting phase differences in multiterminal Josephson junctions*, Phys. Rev. B **90**, 155450 (2014).

[69] M. Coraiola, D. Z. Haxell, D. Sabonis, M. Hinderling, S. C. ten Kate, E. Cheah, F. Krizek, R. Schott, W. Wegscheider, and F. Nichele, *Spin-degeneracy breaking and parity transitions in three-terminal Josephson junctions*, Phys. Rev. X **14**, 031024 (2024).

[70] H. Lee, *Supercurrent and Andreev bound states in multi-terminal Josephson junctions*, Ph.D. thesis, University of Maryland, 2022.

[71] H.-Y. Xie, M. G. Vavilov, and A. Levchenko, *Topological Andreev bands in three-terminal Josephson junctions*, Phys. Rev. B **96**, 161406(R) (2017).

[72] J. S. Meyer and M. Houzet, *Nontrivial Chern numbers in three-terminal Josephson junctions*, Phys. Rev. Lett. **119**, 136807 (2017).

[73] J. Shabani, M. Kjaergaard, H. J. Suominen, Y. Kim, F. Nichele, K. Pakrouski, T. Stankevic, R. M. Lutchyn, P. Krogstrup, R. Feidenhans'l, S. Kraemer, C. Nayak, M. Troyer, C. M. Marcus, and C. J. Palmstrøm, *Two-dimensional epitaxial superconductor–semiconductor heterostructures: A platform for topological superconducting networks*, Phys. Rev. B **93**, 155402 (2016).

[74] E. Cheah, D. Z. Haxell, R. Schott, P. Zeng, E. Paysen, S. C. ten Kate, M. Coraiola, M. Landstetter, A. B. Zadeh, A. Trampert, M. Sousa, H. Riel, F. Nichele, W. Wegscheider, and F. Krizek, *Control over epitaxy and the role of the* InAs/Al *interface in hybrid two-dimensional electron gas systems*, Phys. Rev. Mater. **7**, 073403 (2023).

[75] See Supplemental Material at http://link.aps.org/supplemental/10.1103/qd3y-f912 for additional supporting data and details on the theoretical model (Figs. S1–S9).

[76] Z. Wang and S.-C. Zhang, *Simplified topological invariants for interacting insulators*, Phys. Rev. X **2**, 031008 (2012).

[77] Z. Wang and B. Yan, *Topological Hamiltonian as an exact tool for topological invariants*, J. Phys. Condens. Matter **25**, 155601 (2013).

[78] L. P. Gavensky, G. Usaj, and C. A. Balseiro, *Multi-terminal Josephson junctions: A road to topological flux networks*, Europhys. Lett. **141**, 36001 (2023).

[79] T. Fukui, Y. Hatsugai, and H. Suzuki, *Chern numbers in discretized brillouin zone: Efficient method of computing (spin) Hall conductances*, J. Phys. Soc. Jpn. **74**, 1674 (2005).

[80] M. Z. Hasan and C. L. Kane, *Colloquium: Topological insulators*, Rev. Mod. Phys. **82**, 3045 (2010).

[81] A. Pöschl, A. Danilenko, D. Sabonis, K. Kristjuhan, T. Lindemann, C. Thomas, M. J. Manfra, and C. M. Marcus, *Nonlocal conductance spectroscopy of Andreev bound states in gate-defined* InAs/Al *nanowires*, Phys. Rev. B **106**, L241301 (2022).

[82] N. van Loo, G. P. Mazur, T. Dvir, G. Wang, R. C. Dekker, J.-Y. Wang, M. Lemang, C. Sfiligoj, A. Bordin, D. van Driel, G. Badawy, S. Gazibegovic, E. P. A. M. Bakkers, and L. P. Kouwenhoven, *Electrostatic control of the proximity effect in the bulk of semiconductor-superconductor hybrids*, Nat. Commun. **14**, 3325 (2023).

[83] M.-T. Deng, S. Vaitiekėnas, E. Prada, P. San-Jose, J. Nygård, P. Krogstrup, R. Aguado, and C. M. Marcus, *Nonlocality of Majorana modes in hybrid nanowires*, Phys. Rev. B **98**, 085125 (2018).

[84] A. Danilenko, A. Pöschl, D. Sabonis, V. Vlachodimitropoulos, C. Thomas, M. J. Manfra, and C. M. Marcus, *Spin spectroscopy of a hybrid superconducting nanowire using side-coupled quantum dots*, Phys. Rev. B **108**, 054514 (2023).

[85] T. W. Larsen, K. D. Petersson, F. Kuemmeth, T. S. Jespersen, P. Krogstrup, J. Nygård, and C. M. Marcus, *Semiconductor-nanowire-based superconducting qubit*, Phys. Rev. Lett. **115**, 127001 (2015).

[86] G. de Lange, B. van Heck, A. Bruno, D. J. van Woerkom, A. Geresdi, S. R. Plissard, E. P. A. M. Bakkers, A. R. Akhmerov, and L. DiCarlo, *Realization of microwave quantum circuits using hybrid superconducting-semiconducting nanowire Josephson elements*, Phys. Rev. Lett. **115**, 127002 (2015).

[87] P. Zellekens, R. S. Deacon, P. Perla, D. Grützmacher, M. I. Lepsa, T. Schäpers, and K. Ishibashi, *Microwave spectroscopy of Andreev states in InAs nanowire-based hybrid junctions using a flip-chip layout*, Commun. Phys. **5**, 267 (2022).

[88] M. Hinderling, D. Sabonis, S. Paredes, D. Z. Haxell, M. Coraiola, S. C. ten Kate, E. Cheah, F. Krizek, R. Schott, W. Wegscheider, and F. Nichele, *Flip-chip-based microwave spectroscopy of Andreev bound states in a planar Josephson junction*, Phys. Rev. Appl. **19**, 054026 (2023).

[89] F. J. Matute-Cañadas, L. Tosi, and A. L. Yeyati, *Quantum circuits with multiterminal Josephson-Andreev junctions*, PRX Quantum **5**, 020340 (2024).

[90] T. Antonelli, M. Coraiola, D. C. Ohnmacht, A. Svetogorov, D. Sabonis, S. C. ten Kate, E. Cheah, F. Krizek, R. Schott, J. C. Cuevas, W. Belzig, W. Wegscheider, and F. Nichele, *Exploring the energy spectrum of a four-terminal Josephson junction: Towards topological Andreev band structures*, 10.5281/zenodo.15304098.